ORIGINAL ARTICLE

Characterization of dissimilar aluminum-copper material joining by controlled dual laser beam

Joon Ho Cha[1] · Hae Woon Choi[2]

Abstract

Laser welding affords many advantages during the manufacture of EV battery packs. Aluminum (Al) and copper (Cu) are welded using a dual laser beam with a core and ring of different powers. Given the very high reflectance of Cu and Al exposed to near-infrared lasers, the materials absorb only very small amounts of energy. Compared with single-beam laser welding, dual-beam welding significantly improves the surface quality by controlling surface solidification. Here, we focused on the quality of welded surface beads, the weld properties, and the tensile strength; we varied the output ratio of the core to the ring beam. The optimal conditions for Al6061 were a 700-W core beam, a 500 W ring beam, and a weld speed of 200 mm/s. For C1020P, the optimal conditions were a center beam of 2500 W, a ring beam of 3000 W, and a welding speed of 200 mm/s. During laser lap welding of Al-Al and Al-Cu, the bead width and the interfacial bead width of the joint increased as the output increased. The penetration depth did not significantly change, but small pores formed at the interface of the junction. Tensile tests were performed to demonstrate the reliability of the weld zone; computer simulations were performed to analyze the heat distributions under optimal heat input conditions.

Keywords Laser welding · Battery welding · Dual beam · Dissimilar material · Aluminum/copper welding

1 Introduction

As eco-friendly transportation becomes more important, safety and environmental regulations mandate that all means of transport must be lightweight and highly efficient. In the automobile sector, conventional internal combustion engines are being rapidly replaced by eco-friendly electric and hydrogen engines. Electric vehicles (EVs), hybrid electric vehicles (HEVs), and plug-in hybrid vehicles (PHEVs) require a great deal of power; all feature battery packs composed of hundreds to thousands of cells. Unlike the small batteries of mobile and information technology devices, batteries for vehicles must have high-level capacities and be very reliable, so the production requirements are very high [1–3].

Recently, the need to co-weld dissimilar materials has increased; this can reduce the weight of automobiles and enable fabrication of high-performance, high-quality battery packs. The principal materials used for EV battery pack fabrication are aluminum (Al) and copper (Cu), exploiting the light weight of Al and the high electrical conductivity of Cu. At the cell level, bonding must be very reliable during hermetic welding of tabs and electrodes and cell container cases. At the module level, tab-to-tab and tab-to-busbar connections are required. At the pack level, an excellent joining technique is required to meet the electrical and structural requirements. All of these electrodes, tabs, busbars, and terminals are fabricated from materials that are difficult to weld, including Cu and Al alloys [2, 3].

It is challenging to join dissimilar materials. The melting temperature of aluminum is 660 °C; the melting temperature of copper is 1085 °C. When aluminum melts, the copper remains solid; the dissimilar materials are not joined. Furthermore, laser beam absorption significantly increases when aluminum liquid forms on the surface; the resulting plasma renders welding unstable [1–3].

Current battery-welding techniques include resistance spot-welding, laser, and ultrasonic welding. It is difficult to

✉ Hae Woon Choi
hwchoi@kmu.ac.kr

1 Graduate School of Mechanical Engineering, Keimyung University, Daegu 42601, South Korea

2 Dept. of Mechanical Engineering, Keimyung University, Daegu 42601, South Korea

co-weld dissimilar high-conductivity materials, and laser welding can address this need. When working with Cu and Al, the formation of brittle intermetallic phases (IMPs) compromises battery performance [1]. Laser welding can yield high quality, precision, and productivity with low deformation. Laser welding can be robotized or otherwise automated or mechanized. Formation of hard and brittle intermetallic compounds (IMCs) during joining of dissimilar materials reduces the joining strength [2]. However, laser welding effectively controls IMC formation, facilitating high-quality welding [3, 4].

Laser technologies have found many applications in macro-manufacturing welding, cutting, and marking and have greatly improved the competitiveness of the automobile, shipbuilding, and aviation industries. In terms of microelectronics, laser technologies have improved the productivities and add-on values of semiconductors, displays, and multilayer electronic boards, by making it possible to employ novel composite materials. In short, laser processing is a core technology essential for mass production of high-quality devices because lasers facilitate high-speed precise welding and processing [5, 6].

The reflectances of Cu and Al exposed to a near-infrared laser are very high; the materials absorb very small amounts of energy. Efforts have been made to reduce the thermal effects by creating keyholes in the materials or by using pulsed beams to increase energy absorption [1–6, 25, 26]. Other means of enhancing absorption include laser wobbling or oscillation; in some cases, bonding has employed a brazing technique [1–10, 17]. Recently, green lasers, the energies of which are well-absorbed by Cu, have been developed. Both heat conduction and keyhole welding are possible, because the laser energy absorption of Cu is about 40% at room temperature [8, 9, 25]. Also, welding quality is not affected by the nature of the Cu surface (electropolished, sanded, or a simple plate), and is thus highly reproducible. Such welding finds many applications in battery fabrication.

Laser welding of Al and Cu alloys is difficult because both materials have low melting points, high thermal conductivities, and low-level beam energy absorptions [11–16, 18]. A recently developed dual beam laser operates at a single wavelength (1070 nm), but it is possible to separately control the core and ring beams of a single optical fiber. Compared to single-beam laser welding, dual-beam welding significantly improves surface quality because surface solidification is controlled [18–20, 23]. When multiple beams are used, keyhole formation becomes more stable and spatter is reduced [20–22].

Here, we explore welding of dissimilar materials using a fiber laser that simultaneously outputs core and ring beams. We focused on welding surface bead quality, welding characteristics, and tensile strength, and varied the output ratios of the core and ring beams. We also analyzed heat distribution via computer simulation. Specifically, we evaluated welding characteristics in terms of the surface qualities and shapes of Al-Cu welds, and used simulations to analyze the heat distributions when heat inputs are controlled during welding. Cross-sections of the laser welds were evaluated in terms of process parameters, and welding reliability was verified by measuring the mechanical properties of welds and by noting any defects.

2 Experimental setup and method

2.1 Experimental setup

The fiber laser welding system featured (independently controllable) core and ring beams output by a dual-core optical fiber. Table 1 lists the specifications of the laser system; Fig. 1 presents the experimental setup and schematics of the beam splits. To optimize laser heat input, the two beams were individually controlled; Fig. 2 presents welding specimens and a schematic of the beam delivery system.

Independent control of the core and ring beams allowed welding to proceed in three stages: pre-heating, keyhole formation, and post-heating. During pre-heating, the surface is heated to below the melting point to increase laser energy absorption; this assists melting stability by removing foreign substances. During keyhole formation, a keyhole and a molten pool are formed by the ring and core beams, respectively; these yield a deep, narrow weld bead. Finally, post-heating shortens the length of the keyhole and reduces the molten pool; ultimately, both disappear, with maintained weld stability.

We used 0.4-mm-thick sheets of the Al (Al6061) and Cu (C1020P) alloys typically employed to fabricate EV battery packs. The Al–Si–Mg-based alloy contained about 0.4 to 0.8% silicon (Si) and about 0.8 to 1.2% magnesium (Mg). We employed an oxygen-free copper C1020P-1/2H alloy. Table 2 lists detailed chemical compositions. The sheets were 50 mm in width; Al plates were placed on top of Cu plates for welding. The materials overlapped by 45 mm, and 40-mm sections were welded across the width.

To investigate welding characteristics, bead-on-plate (BOP) tests were performed for both Al and Cu. To

Table 1 Specifications of the laser system

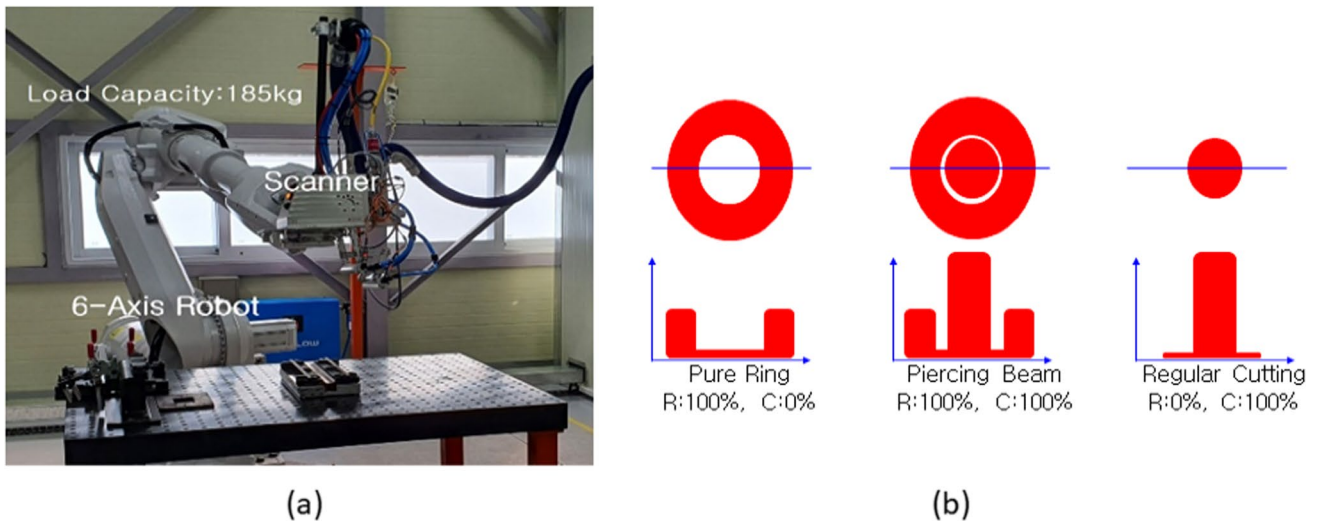| Laser type	FL8000—ARM (fiber laser), Coherent Inc
Wavelength	1.07 μm
Max. power	Center 4 kW, ring 4 kW
Beam modulation	Max. 5 kHz
Optical fiber dia	Center 70 μm, ring 180 μm
Scanner	300 × 200 mm, Fd 560 mm

Fig. 1 Experimental setup. **a** System. **b** Beam split schematic

determine the laser outputs required for full penetration, the output was varied with the welding speed and the focal position was held constant.

2.2 BOP and lap joint welding conditions

Because the properties of the two materials differed, it was necessary to optimize welding [24]. The initial welding conditions were established by fixing the focal position and

welding speed and then varying the laser output. In general, partial penetration welding is required when welding the tabs and busbars of lithium-ion batteries. Given the high reflectivities of Al and Cu alloys, the laser beam was inclined by 8° with respect to the direction of travel, to ensure that the reflected beam did not attain the laser. Lap joint welding was performed in the manner described above, using specimens with dimensions of $100 \times 50 \times 0.4$ mm. The Al specimens were on top and the Cu specimens on the bottom. Welding

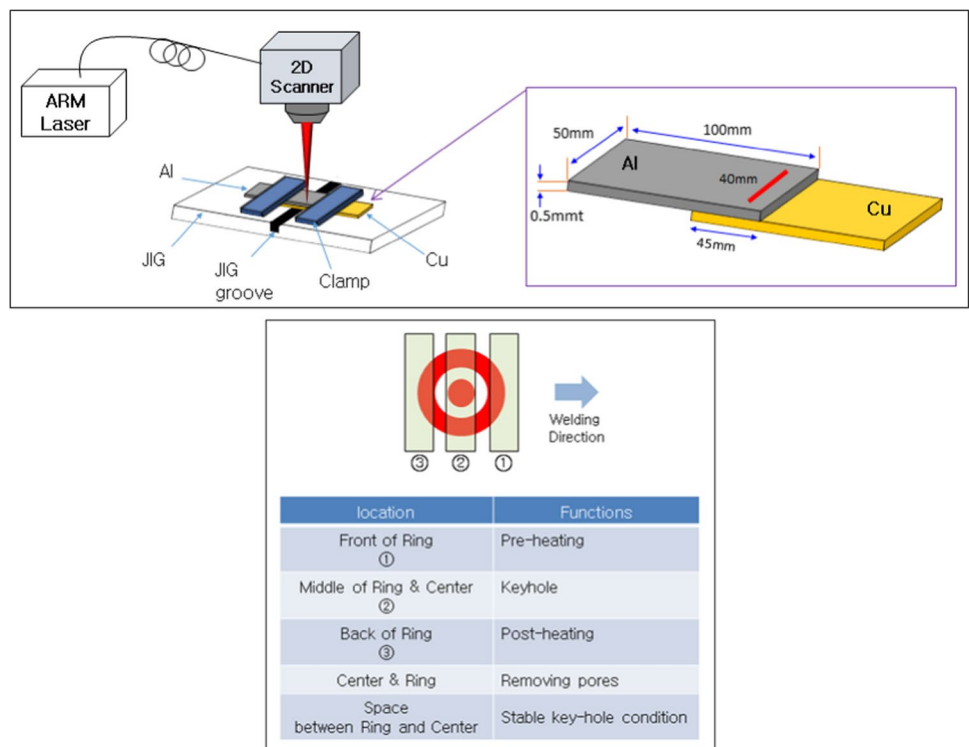**Fig. 2** Laser welding jig and heat input schematic

Table 2 Chemical compositions of the Al and Cu alloy (wt. %)

Material	Cu	Si	Mg	Zn	Mn	Cr	Fe	Ti	Al
Al6061	0.4	0.8	< 1.2	< 0.25	< 0.10	< 0.35	< 0.70	< 0.15	Bal
C1020P			Cu > 99.56		O$_2$ < 10 ppm				

was performed over a length of about 40 mm. The laser light source was remotely irradiated (using a galvanometer scanner). We did not employ a shielding gas supply.

2.3 Computer simulation

To explore the heat distributions when welding Al and Cu, computer simulations were performed with reference to the experimental conditions. Such simulations effectively track weld heat distribution and deformation based on the temperature distribution [11]. When welding dissimilar materials, the optimal heat input can be predicted by simulation to explore how intermetallic compounds (IMCs) with various physical properties affect weld strength and soundness. During typical welding, keyholes are generated, and heat thus moves not only via conduction but also via convection. We used the heat transfer module of COMSOL Multiphysics (ver. 5.3a) for numerical analysis. The simulations were verified by comparing the simulated and actual temperature distributions (the latter were assessed using a thermocouple and an infrared camera).

In the simulations, the Al and Cu plates were of the same thicknesses as those of the experiments; the simulation domain was 40 mm in width and 100 mm in length to allow adequate thermal diffusion. Validation (via computer simulation) was performed as described previously [12]. We placed thermocouples immediately beneath the samples (following the weld lines) and 0.5 mm off the center line.

The governing three-dimensional heat transfer equation for the entire domain is Eq. (1), and the natural convection conditions are given by Eq. (2). The equations were validated as in our prior study and other works [11, 12]:

$$\rho C_p \left(\frac{\partial T}{\partial t} + \mathbf{u}_{trans} \cdot \nabla T \right) + \nabla \cdot (\mathbf{q} + \mathbf{q}_r) = -\alpha T : \frac{dS}{dt} + Q \tag{1}$$

$$\mathbf{q} = -k\nabla T \ or \ h(T_{ext} - T) \tag{2}$$

where Eq. (2) deals with conductive or convective heat transfer through surrounding bodies. In Eq. (2), ρ is the density of the polymer, C_p is the specific heat capacity at constant stress, T is the absolute temperature, $\mathbf{u}_{trans}$ is the velocity vector of translational motion, k is the thermal conductivity, and q is the heat flux of conduction, q_r is the heat flux of radiation, α is the coefficient of thermal expansion, S is the second Piola–Kirchhoff stress tensor, and Q contains the additional laser heat sources of Eq. (3) or (4).

To simulate the core beam, a three-dimensional (3D) Gaussian laser beam was used, as expressed in Eq. (3). The ring beam can be expressed as Eq. (4). The outer and inner diameters of the ring beam were established using the Dirac delta function and the "rectangle function" of COMSOL. Figure 3 presents the 3D models of laser beam intensity distributions for each case.
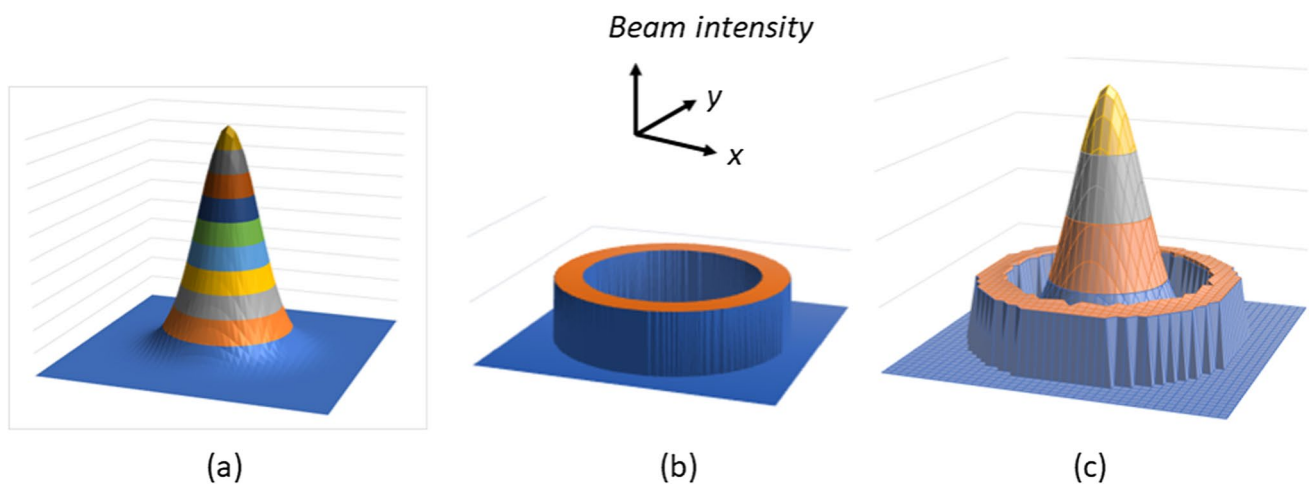

(a)   (b)   (c)

Fig. 3 Laser intensity distribution for (**a**) Gaussian core beam, (**b**) flat top ring beam, and (**c**) combined beam

$$Q(x, y, z) = Q_0(1 - R_c)\frac{A_c}{\pi \sigma_x \sigma_y} e^{-[\frac{(x-x_0)^2}{\sigma_x^2} + \frac{(y-y_0)^2}{\sigma_y^2}]} e^{-[A_c z]} \qquad (3)$$

$$\lim_{\varepsilon \to 0} \int_{x_0-\varepsilon}^{x_0+\varepsilon} \delta(x - x_0) \, dx = 1 \qquad (4)$$

In Eq. (3), Q_0 is the peak power, R_c is the reflectance, σ_x and σ_y are the beam waists in the x and y directions, and A_c is the skin depth/absorption layer thickness. As shown in Eq. (3), the irradiating laser beam was assumed to have a two-dimensional ellipsoidal distribution and a skin depth of A_c in the z direction.

To ensure accurate modeling, we used a fine mesh. Because the diameter of the laser heat source was relatively small compared with the diameter of the entire domain, parametric curves were drawn near the center line to increase the mesh of the heat sources. We used the basic mechanical properties of copper and aluminum. Although some mechanical and optical properties change as the temperature increases [13], laser processing is very rapid and absorption is principally affected by the surface roughness/flatness of the weld pool. Thus, the material and optical properties were assumed to remain constant. A heat transfer module was used for simulation. Conduction and convection equations were applied to the entire domain. In terms of the boundary conditions, the temperature was 293 K and the pressure was 1 atm. Forced air convection was assumed.

A mixed mesh was used to ensure accurate modeling. The minimum element quality was 0.2011; the average quality was 0.6225. The numbers of tetrahedron and triangle meshes were 48,974 and 15,736, respectively. Edge and vertex elements numbered 2473 and 30, respectively.

Skin depth can be analytically calculated for any metal. As a laser beam irradiates a metal, a thin surface layer absorbs laser energy; if the conductivity is high, the absorption is given by Eq. (5) and the penetration depth (or skin depth) is $1/\alpha$. Most common conductors exhibit a relative permeability very close to 1. Thus, for copper and aluminum, a μ value of $4\pi * 10^{-7}$ H/m can be safely assumed.

$$\alpha = \frac{2\omega k}{c_0} \approx \sqrt{\frac{2\sigma_0 \omega}{\varepsilon_0 c_0^2}} \qquad (5)$$

where ω is the angular frequency, k is the wave number, and c_0 is the speed of light. Because the calculated skin depth is very small (at the sub-micron level) and an FEM is thus difficult to apply (because of numerical error), the absorption layer thickness was experimentally determined by comparing Eq. (3) with the temperature measurement.

The reflectance (R_c) is important; it was experimentally determined by integrating the sphere. To track the temperature distribution, a temperature probe was placed 0.5 mm distant from the weld line, and then moved to the upper, middle, and lower surfaces in the direction of thickness.

2.4 Weld tests

To test weld strengths, we performed cross-sectional analyses and mechanical strength tests to assess surface cracks and voids. For weld analysis, the specimens were cut, polished, etched, and observed under a microscope. The Al etching solution was hydrochloric acid 75 mL + nitric acid 25 mL; the Cu etching solution was nitric acid 30 mL + distilled water 70 mL.
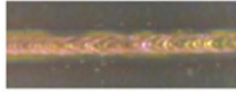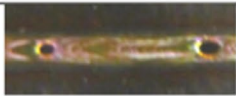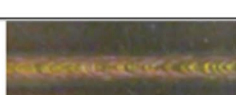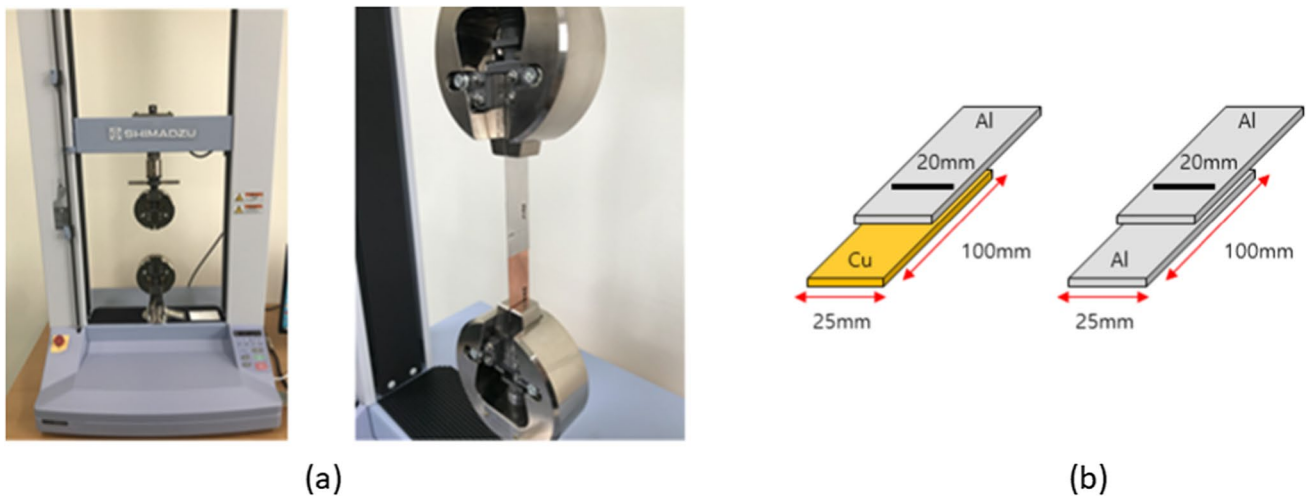

(a)

(b)

Fig. 4 Mechanical property test. **a** Tensile test machine. **b** Test specimen

Fig. 5 BOP experiments for (**a**) aluminum and (**b**) copper material

No.	Laser power(kW)		Speed (mm/sec)	Focus	Bead appearances	Remark
	Core beam	Ring beam				
1-1	1	2	500			over weld
1-2	1	2	200			over weld
2-1	1	1	200	±0		over weld
3-1	0.5	0.5	200			under weld
3-2	0.7	0.5	200			optimum (slope up)

(a)

No.	Laser power(kW)		Speed (mm/sec)	Focus	Bead appearances	Remark
	Core beam	Ring beam				
1-1	3	2	200			over weld
1-2	3	3	200			over weld
2-1	2.5	3	200	±0		partially over weld
2-2	2.5	3	200			optimum (slope up)

(b)

Tensile tests were performed (five replicates for each case) using a 1-tonne-class, small tensile tester (AGS-X; Shimadzu) of grip size about 22 mm. The welding test pieces were cut from the overall test pieces (25–50 mm in width and laser-welded for about 20 mm). Figure 4 presents a photograph of the tensile test system and the specimen specifications.
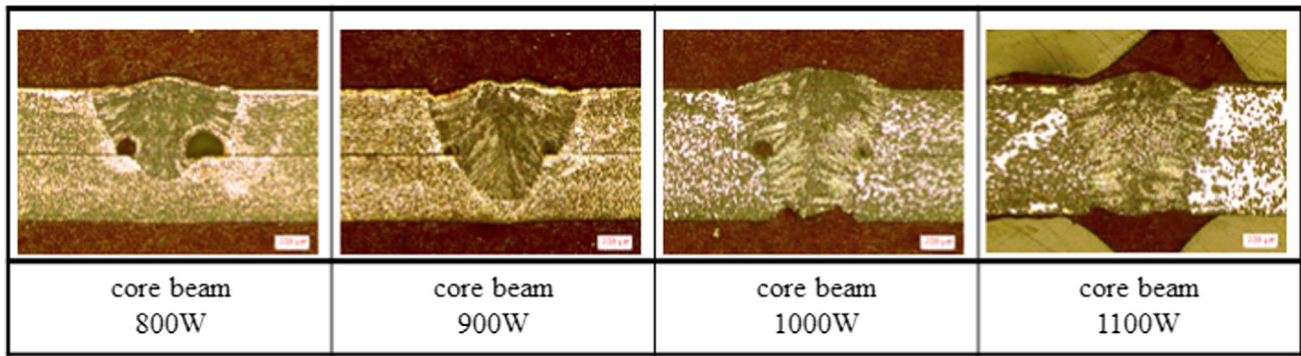
Fig. 6 Cross sectional view of Al-Al welding (ring beam 500 W, speed 200 mm/s)

3 Experimental results and discussion

3.1 BOP characteristics of Al and Cu alloys

We varied the output and welding speeds of the laser core and ring beams to establish appropriate penetration conditions; we performed BOP experiments on separate Al and Cu plates to determine the beam energy absorption rates and thermal diffusions within the materials. The preliminary data that guided the simulations were acquired by observing the bead shape and cross-section of the Al surface by laser power and welding speed. As shown in Fig. 5a, the experiment was performed at welding speeds of 200~500 mm/s; the core and ring beam outputs ranged from 500 to 2000 W.

BOP welding of the Al6061 alloy (thickness 0.4 mm) revealed that welding conditions #1–1 to #2–1 were associated with high heat inputs causing excessive surface and backside beading, as well as melting. The optimal conditions for surface and back bead formation (complete penetration) were 700 W for the core beam, 500 W for the ring beam, and a welding speed of 200 mm/min (thus condition #3–2). The bead width ranged from 0.9 to 1.0 mm, and the computer simulation was based on these results.

Figure 5b presents the BOP welding conditions and macrophotographs revealing surface bead quality for the C1020P test material. Excessive discontinuity was evident early in welding of specimens #1–1, #1–2, and #2–1. To avoid this, we set the output slope to 1 mm to ensure that the laser beam did not interfere with keyhole welding of a substrate with a high reflectance and low beam absorption. For BOP welding of the C1020P alloy (thickness 0.4 mm), the optimal conditions for formation of a sound surface and back beads (reflecting full penetration) were a core beam of 2.5 kW, a ring beam of 3 kW, and a welding speed of 200 mm/min.

The optimal conditions were thus those of #3–2 and #2–2, which eliminated discontinuity defects via output slope control early in welding. As shown in Fig. 5, for the soft

Al6061 specimen, a hole (a "piercing") occurred early during welding, but a sound bead formed later when the output stabilized.

3.2 Lap joint welding of homogeneous Al-Al materials

Figure 6 presents the laser lap-welding results and cross-sectional views of homogeneous Al-Al materials. Welding proceeded by increasing the core beam output in 100 W steps from 800 to 1100 W, with adjustment of the ring beam output. As the laser power increased, so did the bead width and penetration depth; pores developed when partial penetration occurred at 800–1000 W. This likely reflects the fact that gas in the weld does not escape during high-speed aluminum welding. If full penetration is in play, gas is discharged from below even if pores are generated. As shown in Fig. 6, some pores were evident at the boundaries after low-heat-input welding; they vanished as the heat input increased. The optimal cross-sectional result was afforded by 1100-W core beam welding.

Figure 7 presents the bead widths and penetration depths for each position. To objectively compare the weld cross-sections, we investigated the relationships between the welding conditions and penetration depth (P_t), surface bead width (B_t), overlap joint bead width (B_m), and back bead width (B_b). Figure 7a defines the geometrical terms used to describe the weld shapes and positions; Fig. 7b shows that when welding proceeded as the center beam output rose in 100-W steps, the width of the upper bead was not significantly affected, but the penetration depth increased. This did not significantly increase the upper bead width because the laser beam was initially largely reflected from the Al surface.

Figure 7c presents the tensile strengths obtained when the core beam output was changed, with the ring beam, welding speed, and focus fixed. The tensile load increased slightly as the width of the upper bead increased, because the heat
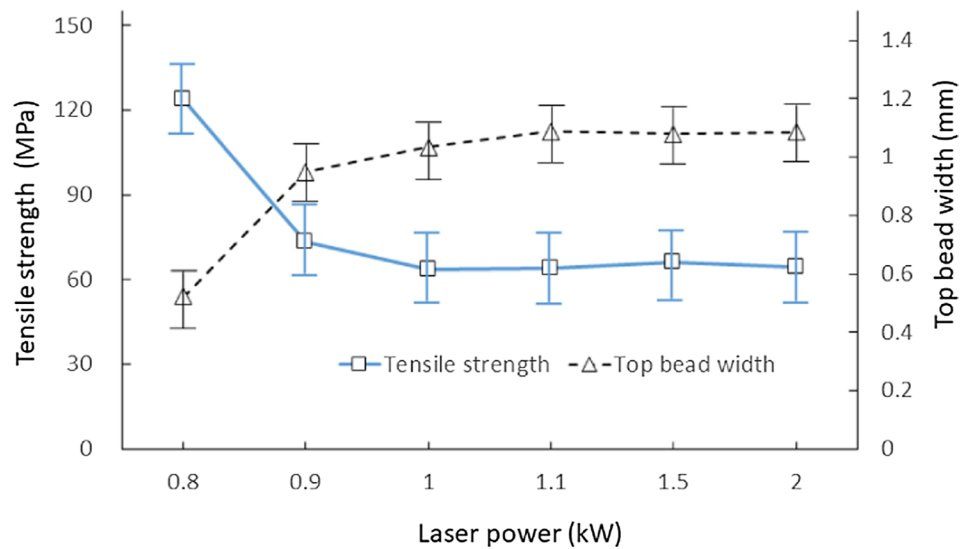
Fig. 7 a Definition of weld geometry. **b** Weld bead measurement according to laser power. **c** Tensile test results for aluminum-aluminum welding by various heat input
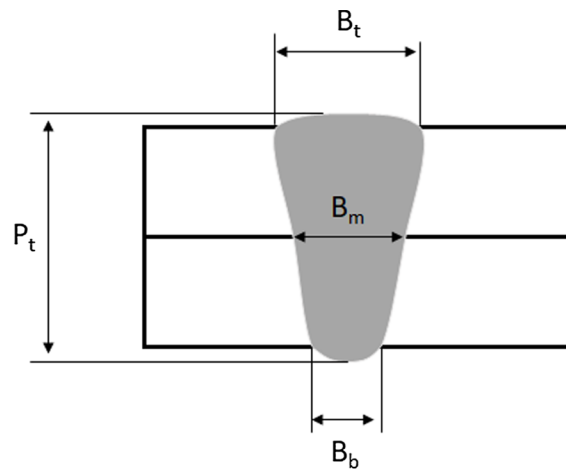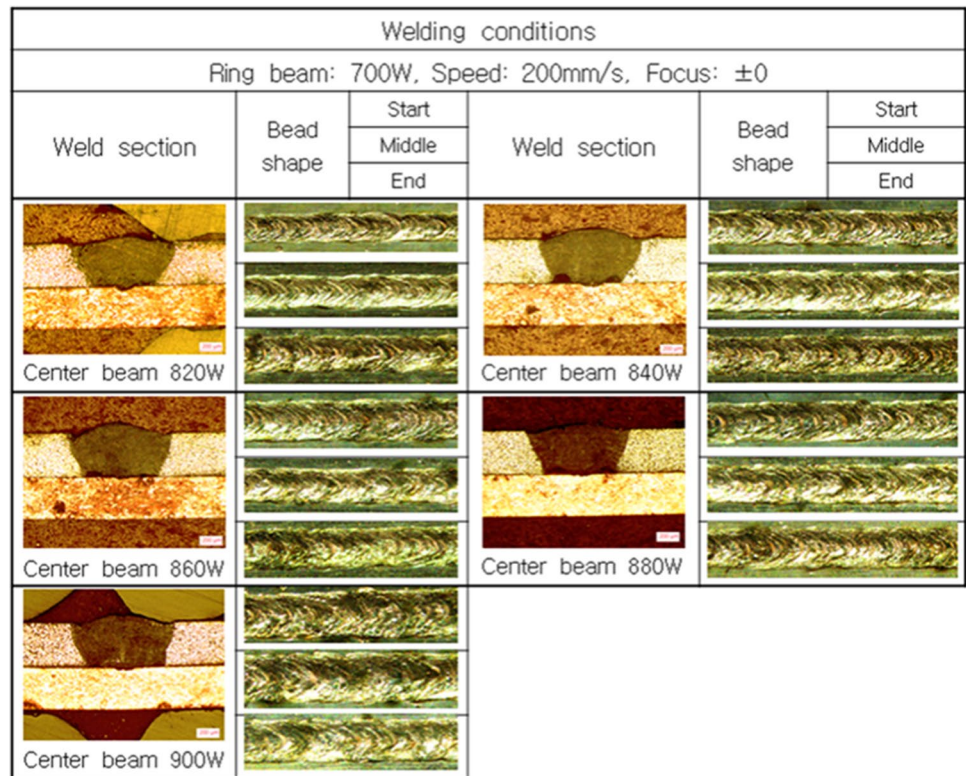

(a) Definition of weld geometry
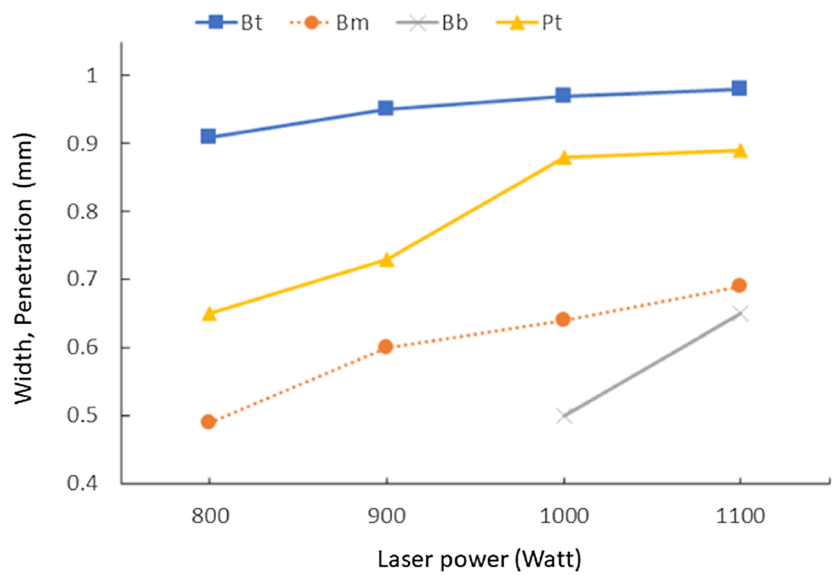
(b) Weld bead measurement according to laser power

(c) Tensile test results for aluminum-aluminum welding by various heat input

Fig. 8 Cross-sections of aluminum and copper welding

3.3 Surface and cross-sectional analysis of overlapping Al-Cu welds

Figure 8 presents the results of laser lap Al-Cu welding. The ring beam output (700 W), welding speed (200 mm/s), and focal position (± 0) were fixed; the center beam intensity was

input rose when the same metals were welded. However, the tensile strength decreased as the bead width increased, attributable to failure of the base material. No damage was attributable to any feature of the weld.

increased in 20-W steps from 820~900 W and the shapes of the welds were examined. As the output increased, the surface bead width (B_t) and the junction interface bead width (B_m) increased, attributable to the reflectivity of Cu. Even when the center beam passed through the Al6061 test piece, the output did not affect penetration, given the low absorptivity of C1020P.

Similar to aluminum-to-aluminum welding, some pores were evident at the boundaries after low-heat-input welding; however, these vanished with increasing heat input. The optimal cross-sectional result was afforded by a core/center beam of 880 W.

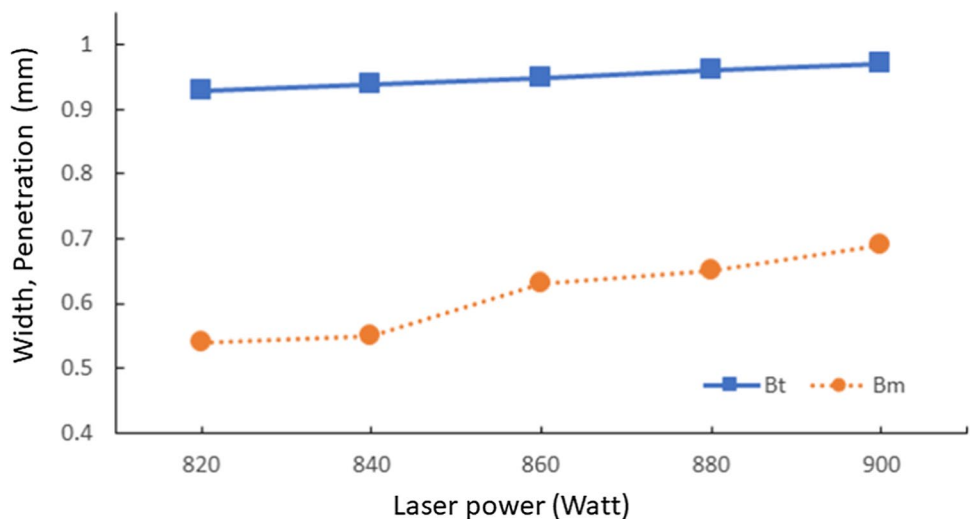**Fig. 9** Effect of laser power on bead formation for aluminum-copper welding
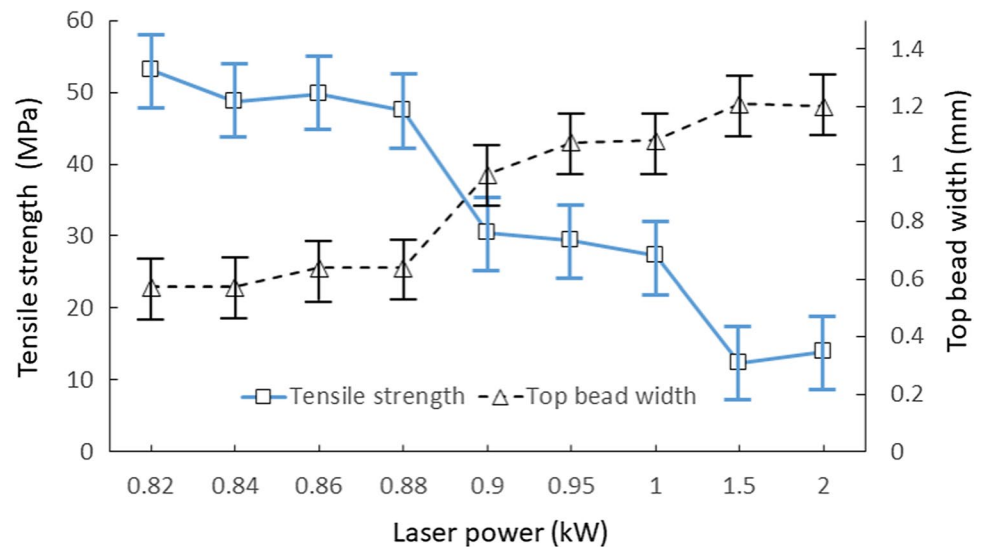
Fig. 10 Tensile test results for aluminum-copper welding by various heat input

Brittle IMCs generated et al.-Cu interfaces impair weld strength, as do small pores in joints. Figure 9 presents the widths of the Al-Cu laser junctions. The width of the interface between the surface bead and the joint tended to increase as the output increased, as also seen when Al was welded. Because the penetration was only partial, the back bead width and penetration depth were not available. Cross-sectional analysis revealed that the interface between C1020P and Al6160 was appropriate.

3.4 Tensile strengths of real welds and computer simulations

To explore the tensile strength by welding output, the core beam output was varied from 800 to 2000 W with the ring beam held at 700 W, the welding speed at 200 mm/s, and the focal position at ± 0. During the tensile strength tests, 5 replicates were used at each laser power. Figure 10 presents the tensile test data on upper bead widths. The tensile load was set to 62 kg$_f$ at 820 W, corresponding to a tensile strength

of 55 MPa; this did not increase when the welding power increased. However, the surface bead width increased as the welding power increased. After tensile testing, we found interfacial fractures of the Al-Cu interfaces in all specimens. We presume that these were brittle fractures, as suggested by the scatter diagram of tensile strength. In the 1500 W and 2000 W tensile tests, most of the upper Al6061 welds fell onto the lower C1020P welds. Thus, the IMC thickness was excessive given the large heat input.

Computer simulation was conducted to estimate the heat distributions by the heat input ratios of the core and ring beams. We tested ratios of 1200/0 W, 0/1200 W, and 700/500 W of core/ring-beam power. As shown in Fig. 11, when the total heat input was that of the core beam, the maximum temperature was 576 °C; when the total heat input was that of the ring beam, the maximum temperature was 1360 °C. However, experimentally, the maximum temperature was 860 °C when the core/ring beam ratio was appropriate, thus allowing good temperature control.
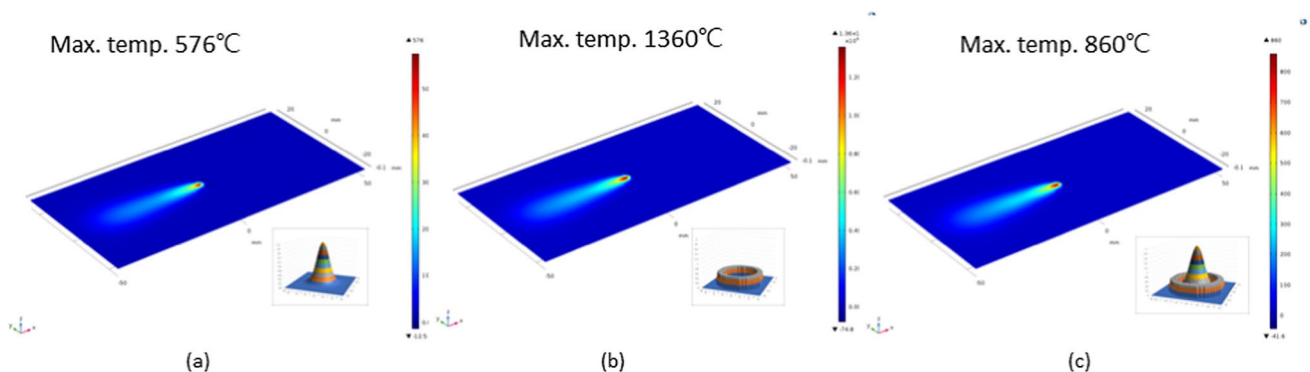

Fig. 11 Computer simulation for core/ring. **a** 1200 W/0 W. **b** 0 W/1200 W. **c** 700 W/500 W

Fig. 12 Heat distribution at various heat inputs, C-core beam, R-ring beam
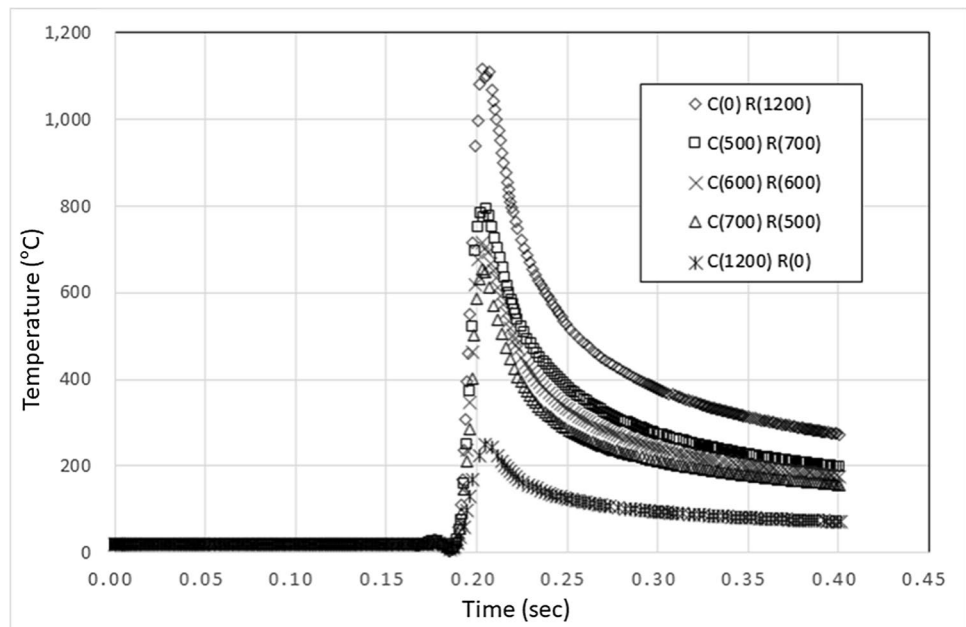

Figure 12 presents the simulation results as the core/ring beam ratio varied. During simulation, the core and ring beams ranged from 0 to 1200 W but their sum was always 1200 W. Temperatures were calculated 0.5 mm distant from the center of the weld bead interface. In conclusion, we found that the ring beam output determined the size of the weld bead surface.

4 Conclusions

We studied the characteristics of Al/Cu weld joints formed using separately controllable core and ring beams. We performed BOP tests on Al, Cu, homogeneous Al-Al materials, and heterogeneous Al-Cu materials. The heat distributions were analyzed via computer simulation. The conclusions are as follows:

1. In terms of BOP welding of Al6061 and C1020P materials, the optimal conditions were a core beam of 700 W, a ring beam of 500 W, and a welding speed of 200 mm/s for Al6061. For C1020P, the optimal conditions were a center beam of 2500 W, a ring beam of 3000 W, and a welding speed of 200 mm/s. Some initial welding defects could be eliminated via output slope control.
2. On laser lap welding of Al-Al and Al-Cu, the bead width and the interfacial bead width at the junction increased when the output increased. The penetration depth did not vary markedly, but small pores formed at the interface of the junction.
3. For homogeneous Al-Al materials, as the laser power increased, all of the upper bead width, joint interface bead width, and penetration depth tended to increase. However, welds associated with low heat inputs exhibited pores caused by partial penetration, but healthy welds without pores formed after full penetration.
4. Tensile tests on the heterogeneous material revealed that the tensile strength did not increase as the welding power increased, remaining at about 55 MPa. The tensile strength fell to about 10 MPa at high energy inputs (1.5 and 2.0 kW) because of IMC formation at the interface of the weld; this heat input was excessive.

Author contribution HC: conceptualization, writing-review and editing, experiment review; JC: experiment, formal analysis, data curation, writing—original draft preparation; All authors have read and agreed to the published version of the manuscript.

Data availability The datasets generated during and/or analyzed in the current study are available from the corresponding author on reasonable request.

Declarations

Ethics approval Not applicable.

Consent to participate   Not applicable.

Consent for publication   Not applicable.

Conflict of interest   The authors declare no competing interests.

References

1. Mathivanan K, Plapper P (2019) Laser Welding of dissimilar copper and aluminum sheets by shaping the laser pulses. Procedia manufacturing 36:154–162. https://doi.org/10.1016/j.promfg.2019.08.021
2. Miller WS, Zhuang L, Bottema J et al (2000) Recent development in aluminium alloys for the automotive industry. Mater Sci Eng, A 280(1):37–49. https://doi.org/10.1016/S0921-5093(99)00653-X
3. Schubert E, Zerner I, Sepold G (1997) Laser beam joining of material combinations for automotive applications. Proc SPIE 3097:212–220. https://doi.org/10.1117/12.281079
4. Gao M, Chen C, Mei S et al (2014) Parameter optimization and mechanism of laser–arc hybrid welding of dissimilar Al alloy and stainless steel. Int J Adv Manuf Technol 74:199–208. https://doi.org/10.1007/s00170-014-5996-z
5. Hung CH, Chen WT, Sehhat MH et al (2021) The effect of laser welding modes on mechanical properties and microstructure of 304L stainless steel parts fabricated by laser-foil-printing additive manufacturing. Int J Adv Manuf Technol 112:867–877. https://doi.org/10.1007/s00170-020-06402-7
6. Xu Y, Gong Y, Li P et al (2020) The effect of laser power on the microstructure and wear performance of IN718 superalloy fabricated by laser additive manufacturing. Int J Adv Manuf Technol 108:2245–2254. https://doi.org/10.1007/s00170-020-05172-6
7. Wang P, Chen X, Pan Q et al (2016) Capacity optimization in Industry Laser welding dissimilar materials of aluminum to steel: an overview. Int J of Adv Manuf Technol 98:9–12. https://doi.org/10.1007/s00170-016-8725-y
8. Punzel E, Hugger F, Dorringer R et al (2020) Comparison of different system technologies for continuous-wave laser beam welding of copper. Procedia CIRP 94:587–591. https://doi.org/10.1016/j.procir.2020.09.081
9. Kick M, Habedank J, Heilmeier J et al (2020) Contacting of 18650 lithium-ion batteries and copper bus bars using pulsed green laser radiation. Procedia CIRP 94(94):577–581. https://doi.org/10.1016/j.procir.2020.09.079
10. Schmalen P, Plapper P (2016) Evaluation of laser braze-welded dissimilar Al-Cu joints. Phys Procedia 83:506–514. https://doi.org/10.1016/j.phpro.2016.08.052
11. Hartel U, Ilin A, Bantel C, Gibmeier J et al (2016) Finite element modeling for the structural analysis of Al-Cu laser beam welding. Phys Procedia 83:1404–1414. https://doi.org/10.1016/j.phpro.2016.08.147
12. Choi S, Choi H (2021) Parametric analysis of thermal effects on multi layered laser welding. Journal of the Korean Society of Manufacturing Process Engineers 20(8):18–24. https://doi.org/10.14775/ksmpe.2021.20.08.0018
13. Garnov S, Konov V, Silenok A et al (1997) Experimental study of temperature dependence of reflectivity and heat capacity of steels and alloys at continuous wave Nd:YAG laser heating. Proc SPIE Int Soc Opt Eng. https://doi.org/10.1117/12.271672
14. Garavaglia M, Demir A, Zarini S et al (2020) Fiber laser welding of AA 5754 in the double lap-joint configuration: process development, mechanical characterization and monitoring. Int J of Adv Manuf Technol 111:1643–1657. https://doi.org/10.1007/s00170-020-06128-6
15. Reisgen U, Olschok S, Jakobs S et al (2018) Influence of the degree of dilution with laser beam vacuum-welded Cu-Al mixed joints on the electrical properties. Procedia CIRP 74(74):23–26. https://doi.org/10.1016/j.procir.2018.08.022
16. Zhou X, Zhang G, Shi Y et al (2017) Microstructures and mechanical behavior of aluminum-copper lap joints. Mater Sci Eng A 705:105–113. https://doi.org/10.1016/j.msea.2017.08.056
17. Brand M, Schmidt P, Zaeh M et al (2015) Welding techniques for battery cells and resulting electrical contact resistances. J Energy Storage 1:7–14. https://doi.org/10.1016/j.est.2015.04.001
18. Chen S, Zhai Z, Huang J et al (2015) Interface microstructure and fracture behavior of single/dual-beam laser welded steel-Al dissimilar joint produced with copper interlayer. Int J of Adv Manuf Technol 83:1–4. https://doi.org/10.1007/s00170-015-7390-x
19. Bono P (2015) Laser welding of copper and aluminum battery interconnections. Proceedings Industrial Laser Applications Symposium 9657. https://doi.org/10.1117/12.2176048
20. Kah P, Vimalraj C, Martikainen J et al (2015) Factors influencing Al-Cu weld properties by intermetallic compound formation. Int J Mech Mater Eng 10:1. https://doi.org/10.1186/s40712-015-0037-8
21. Coroado J, Meco1 S, Williams S et al (2017) Fundamental understanding of the interaction of continuous wave laser with aluminum. Int J Adv Manuf Technol 93:3165–3174. https://doi.org/10.1007/s00170-017-0702-6
22. Franciosa P, Serino A, Al Botros R et al (2019) Closed-loop gap bridging control for remote laser welding of aluminum components based on first principle energy and mass balance. J Laser Appl 31:022416. https://doi.org/10.2351/1.5096099
23. Hietala M, Hamada A, Keskitalo M et al (2020) Mechanical characterization of laser-welded double-lap joints in ultra-high and low strength steels for sandwich panel applications. Mater Today Proc 28:455–460. https://doi.org/10.1016/j.matpr.2019.10.031
24. Elefante A, Nilsen M, Sikström F et al (2019) Detecting beam offsets in laser welding of closed-square-butt joints by wavelet analysis of an optical process signal. Opt Laser Technol 109:178–185. https://doi.org/10.1016/j.optlastec.2018.08.006
25. Kim T, Choi H (2021) Study on laser welding of Al-Cu dissimilar material by green laser and weld quality evaluation by deep learning. Journal of Welding and Joining 39:67–73. https://doi.org/10.5781/JWJ.2021.39.1.8
26. You H, Kang M, Yi S et al (2021) Modeling of laser welds using machine learning algorithm. Journal of Welding and Joining 39:36–44. https://doi.org/10.5781/JWJ.2021.39.1.4